Mottness Collapse in 1T-$TaS_{2-x}Se_x$ Transition-Metal Dichalcogenide: An Interplay between Localized and Itinerant Orbitals

Shuang Qiao,[1,2] Xintong Li,[1] Naizhou Wang,[3] Wei Ruan,[1] Cun Ye,[1] Peng Cai,[1] Zhenqi Hao,[1] Hong Yao,[2,4] Xianhui Chen,[3,5] Jian Wu,[1,4,*] Yayu Wang,[1,4,†] and Zheng Liu[2,4,‡]

[1]*State Key Laboratory of Low Dimensional Quantum Physics, Department of Physics, Tsinghua University, Beijing 100084, People's Republic of China*
[2]*Institute for Advanced Studies, Tsinghua University, Beijing 100084, People's Republic of China*
[3]*Hefei National Laboratory for Physical Science at Microscale and Department of Physics, University of Science and Technology of China, Hefei, Anhui 230026, People's Republic of China*
[4]*Innovation Center of Quantum Matter, Beijing 100084, People's Republic of China*
[5]*Collaborative Innovation Center of Advanced Microstructures, Nanjing University, Nanjing 210093, China*

(Received 25 March 2017; published 1 December 2017)

The layered transition-metal dichalcogenide 1T-TaS_2 has been recently found to undergo a Mott-insulator-to-superconductor transition induced by high pressure, charge doping, or isovalent substitution. By combining scanning tunneling microscopy measurements and first-principles calculations, we investigate the atomic scale electronic structure of the 1T-TaS_2 Mott insulator and its evolution to the metallic state upon isovalent substitution of S with Se. We identify two distinct types of orbital textures—one localized and the other extended—and demonstrate that the interplay between them is the key factor that determines the electronic structure. In particular, we show that the continuous evolution of the charge gap visualized by scanning tunneling microscopy is due to the immersion of the localized-orbital-induced Hubbard bands into the extended-orbital-spanned Fermi sea, featuring a unique evolution from a Mott gap to a charge-transfer gap. This new mechanism of Mottness collapse revealed here suggests an interesting route for creating novel electronic states and designing future electronic devices.

DOI: 10.1103/PhysRevX.7.041054

Subject Areas: Condensed Matter Physics, Materials Science, Strongly Correlated Materials

I. INTRODUCTION

The vicinity of a Mott insulating phase has constantly been a fertile ground for finding exotic quantum states, most notably the high T_c cuprates and colossal magnetoresistance manganites. The layered transition-metal dichalcogenide 1T-TaS_2 represents another intriguing example. More interestingly, it has been recently found that 1T-TaS_2 undergoes a Mott-insulator-to-superconductor transition induced by high pressure [1], charge doping [2–5], or isovalent substitution [6–8].

The nature of the Mott insulator phase and transition mechanism to the conducting state is still under heated debate. Much of the challenge originates from a series of complicated charge-density wave (CDW) orders entwined with the electronics phases [9–11]. The Mott insulator phase is believed to be a consequence of the commensurate CDW (CCDW) order [11–15]. Superconductivity emerges as the Mott insulator state is suppressed, and the electronic phase diagram [1,4,5,7] displays many similarities to that of the cuprates.

Different scenarios were proposed to account for the Mott-insulator-to-superconductor transition. For the pressurization case, it was assumed that the superconductivity formed within the metallic interdomain spaces of the nearly commensurate CDW (NCCDW) phase [1]. This scenario is consistent with the phase separation picture of the NCCDW phase [16]. It also naturally explains the continuous extension of superconductivity into the incommensurate CDW phase, where the interdomain spaces grow to the whole sample and the CCDW domains completely disappear. On the other hand, for the chemical doping cases, angle-resolved photoemission measurements did not reveal any signature of phase separation [3], suggesting instead strong electronic hybridization across domains. The electrons were found to form a global melted Mott state with a single electron pocket around the Γ point, from which superconductivity could emerge. Another perspective on the melted Mott state was recently developed by viewing

*wu@phys.tsinghua.edu.cn
†yayuwang@tsinghua.edu.cn
‡zheng-liu@tsinghua.edu.cn

doped 1T-TaS_2 as a disordered Mott insulator [17], in which the interplay of strong interaction and disorder generates a novel pseudogap metallic state.

Most of the previous explanations were essentially based on a one-band Hubbard model [17–19], and the efforts were made to reproduce the phase transition by tuning some parameters. The problems, however, are that the microscopic meaning of the one-band basis is ambiguous, and the dependence of the associated parameters on the material details is unclear. Consequently, it heavily relies on the researcher's perspective to select the key parameters and the tuning range. This leads to rather controversial interpretations emphasizing different aspects of the material [1,3,6,8,17,20–25], such as spin-orbit coupling, interlayer coupling, *p-d* hybridization, and disorder.

Scanning tunneling microscopy (STM) or scanning tunneling spectroscopy is an ideal experimental technique for probing the atomic scale electronic structure of complex materials. Recent STM experiments on the pristine 1T-TaS_2 [24] and its pulses-induced states [26,27] have revealed interesting spectral features due to the interplay of CDW and electron correlation. In particular, both the CDW and Mott gap can be clearly resolved. On the other hand, first-principles calculation based on the density-functional theory (DFT) renders an efficient simulation starting from a complete microscopic description of the material. It is understood that only approximate calculation methods can work for such a strongly correlated system with a large unit cell. Previous DFT calculation [28] with an on-site Coulomb repulsion correction ($+U$) has shown that the Mott gap of the pristine 1T-TaS_2 can be reasonably described, although it inevitably suffers from an oversimplified mean-field treatment of electronic correlation. We will employ the same methodology for the Se-substitute 1T-TaS_2. Compared with the empirical model calculation, such as tight binding or the one-band Hubbard model solved using the dynamic mean-field approximation, the advantage of DFT + U is that the interorbital hybridization and spillover associated with the CDW order are self-consistently captured without tunable parameters. This property is considered to be particularly important in our Se-substitution experiment. Moreover, the DFT + U calculation can be used to map out a realistic minimal effective model and specify the parameters, as we present in the end, which may be later studied by methods with a more sophisticated treatment of electronic correlation.

The aim of the present article is to establish a concrete foundation that describes the low-energy physics in 1T-TaS_2. By combining STM measurements and *ab initio* Wannier function analysis, we single out two distinct types of orbital textures and formulate a multiorbital effective Hamiltonian based on these two orbital textures. This construction reveals a new origin of the Mott-insulator-to-superconductivity transition in 1T-TaS_2. We map out the complete transition process by inhomogeneous Se substitution, and demonstrate an excellent agreement between experiment and theory. The remainder of the article is organized as follows. Section II describes the experiment and calculation methods. Section III presents the STM and first-principles data on pristine TaS_2, based on which the two types of most relevant orbital textures are identified. Section IV discusses results on Se-substituted samples. By taking advantage of the chemical inhomogeneity in these samples, we map out the complete collapsing process of the Mott phase. Section V discusses the theoretical formalism of the transition in details. Section VI concludes this article.

II. EXPERIMENT AND CALCULATION METHODS

The high-quality single crystals of 1T-$TaS_{2-x}Se_x$ ($0 < x < 2$) are synthesized by the chemical vapor transport method with iodine as the transport agent. The powder of Ta, S, and Se is weighted stoichiometrically and thoroughly grounded. Then the mixture together with 150 mg I_2 is sealed into an evacuated quartz tube and placed into a two-zone furnace with the temperature gradient of 1253–1153 K for 1 week. The products are washed with ethanol to remove the iodine at the surface.

The STM experiments are performed with a cryogenic variable-temperature ultrahigh vacuum STM system. The 1T-$TaS_{2-x}Se_x$ crystal is cleaved *in situ* at $T = 77$ K, and the measurement is taken at 5 K with an electrochemically etched tungsten tip calibrated on a clean Au (111) surface [29]. The STM topography is taken in the constant current mode, and the dI/dV spectra are obtained with a standard lock-in technique with modulation frequency $f = 423$ Hz. To obtain the differential conductance dI/dV maps shown in Fig. 2, we take the dI/dV measurement on a spatial grid (x, y) of that area with the same setup parameters (tunneling current $I_t = 20$ pA and bias voltage $V_{\text{set point}} = -2$ V), and extract the conductance map for a given bias voltage from the three-dimensional data set dI/dV (V_b, x, y).

The first-principles calculation based on the density-functional theory is performed using the Vienna *ab initio* simulation package [30–33] with a 280-eV plane-wave basis cutoff. The Perdew-Burke-Ernzerhof generalized gradient approximation [34] and the projector augmented wave method [35] are employed. The Wannier function analysis is performed using the WANNIER90 code [36–38] on the plain DFT level in order to quantify the single-electron properties, such as *p-d* hybridization and interatomic hopping. The $+U$ correction is employed to compare with the STM dI/dV spectra, which captures the Coulomb interaction of Ta $5d$ orbitals on the mean-field level, following the simplified (rotational invariant) approach introduced by Dudarev [39,40]. The Mott gap depends on the choice of the $+U$ parameter. We employ U-J = 2.27 eV as previously derived from the linear-response calculation for pure 1T-TaS_2 [28], which was found to nicely reproduce the experimental Mott gap. We employ the lattice parameters determined by experiment [41], and

relax the atomic coordination self-consistently until the forces are less than 0.002 eV/Å. To simulate the CCDW order, we employ a $\sqrt{13} \times \sqrt{13}$ supercell consisting of 13 Ta atoms forming a Star of David (SD) structure. The integration over the Brillouin zone is obtained on a Γ-centered $6 \times 6 \times 1$ k mesh. The electronic self-consistent iterations are converged to 10^{-5} eV precision of the total energy.

All our calculations are based on a 2D structural configuration with a 15-Å-thick vacuum space to eliminate coupling between different layers. It has been shown by earlier studies that at least for band structure effects alone, 1T-TaS_2 should always be describable as a quasi-two-dimensional system [11,42]. Indeed, recent calculations [25] emphasizing the interlayer orbital texture showed that the Mott-insulating ground state cannot be correctly reproduced once an artificial c-axis stacking sequence is imposed. On the other hand, in 1T-$TaSe_2$ interlayer coupling plays a more important role [43]. Therefore, we restrict our discussion within the S-riched regime, and focus on the *intralayer* CCDW order and orbital textures.

III. ORBITAL TEXTURES IN PRISTINE TaS_2

A. Structural and electronic properties

1T-TaS_2 has a layered structure as shown in Fig. 1(a), in which the Ta atoms form a planar triangular lattice sandwiched by two S-atom planes. Figure 1(b) displays the STM topographic image of pristine 1T-TaS_2, which clearly reveals the CCDW order with a $\sqrt{13} \times \sqrt{13}$ superlattice where 13 Ta atoms form a SD structure. Note that the bright spots correspond to the S atoms lying in the uppermost layer, and the position of the Ta atoms can be determined according to the octahedral coordination. While the Ta layer has sixfold rotation symmetry, the top or bottom S layer has only threefold symmetry. In Fig. 1(c), we show the spatially averaged differential conductance dI/dV, which is approximately proportional to the electron density of states (DOS), of pristine 1T-TaS_2. An energy gap around the Fermi level (E_F) can be clearly observed, which is attributed to the Mott-Hubbard gap of the insulating CCDW phase, as previously determined in Ref. [24].

These spectroscopic features can be captured by DFT calculations including the on-site Hubbard U correction in a Hartree-Fock manner [28]. As shown in Fig. 1(d), there is a full charge gap around the (E_F), which is bounded by two narrow bands, corresponding to the upper and lower Hubbard bands (UHB and LHB), respectively. There is another energy gap below the LHB isolating it from the underneath dispersive valence band (VB) continuum [shaded in blue in Fig. 1(d)], which is commonly referred to as the CDW gap (Δ_{CDW}) [44–46]. This gap is manifested in the dI/dV spectrum as a dip below the LHB [Fig. 1(c)].

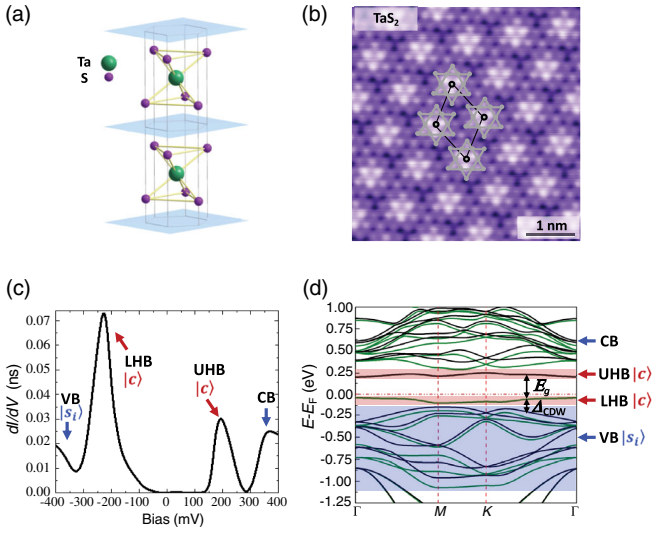

FIG. 1. Structural and electronic properties of 1T-TaS_2. (a) Crystal structure of 1T-TaS_2. (b) Atomic resolved topographic image of 1T-TaS_2 with bias voltage $V_b = 1$ V and tunneling current $I_t = 20$ pA. Each bright site on the surface corresponds to a S atom in the topmost layer. The gray dots and the black lines mark the SD structure and the CCDW superlattice, respectively. The crystal cleaves easily between two adjacent S layers, as indicated by the blue planes in (a), exposing the triangular lattice of S atoms. (c) Spatial averaged STM dI/dV spectrum acquired at 5 K. (d) DFT + U band structure of 1T-TaS_2. The black and green colored curves represent the two spin components. The shaded regions indicate the energy range belonging to the different orbitals.

B. Low-energy orbital textures and their origin

Besides the CCDW superstructure and energy spectrum, equally important is the local DOS (LDOS) mapping at selected energies, which contains the spatial characteristics of electronic wave functions, i.e., the orbital texture. Figure 2(a) displays the dI/dV, or LDOS, mapping measured at two representative energies. At $V_b = -207$ mV (upper panel), which corresponds to the LHB, the LDOS map shows a periodic pattern that is commensurate with the CCDW superlattice. By comparing the LDOS map with the topographic image [Fig. 1(b)], the bright spots are identified to be the center of SDs. Moving to lower energy with bias $V_b = -422$ mV (lower panel), a distinctly different orbital texture is revealed for the VB: the LDOS map exhibits a honeycomblike superstructure. Its bright or dark spots are the inverse of the previous texture, indicating contributions mainly from the surrounding Ta orbitals. LDOS maps at positive biases give a nearly symmetric picture, demonstrating the same two types of orbital textures: the UHB $V_b = 199$ mV [Fig. 2(c) upper panel] corresponds to an orbital texture concentrated on the center of SDs, whereas at higher energy $V_b = 484$ mV [Fig. 2(c) lower panel] for the conduction bands (CB), the bright spots shift to the surrounding Ta orbitals.

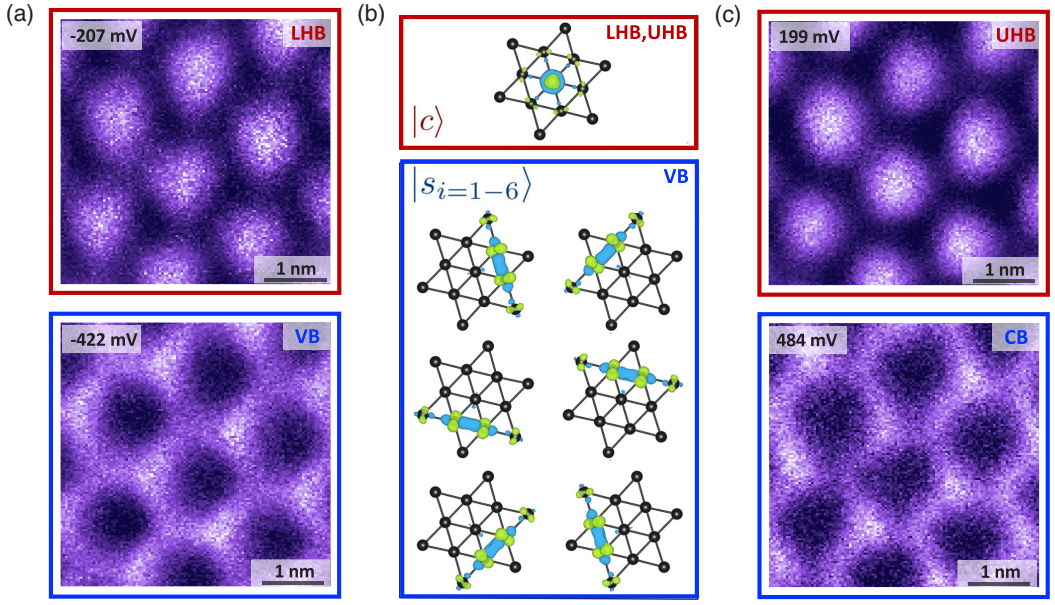

FIG. 2. Two types of orbital textures in 1T-TaS_2. (a) [(c)] Differential conductance (dI/dV) maps (42×42 Å^2) measured at $V_b = -207$ [199] mV (up) and $V_b = -422$ [484] mV (bottom) with tunneling current $I_t = 20$ pA, and the setpoint bias voltage for all the maps is $V_s = -2$ V. The center of each CDW cluster is brighter at -0.2 [0.2] V while the edges are brighter at -0.4 [0.4] V. (b) Isovalue surface of the two types of Wannier functions.

To determine the nature of these two orbital textures discussed above, we proceed by performing *ab initio* Wannier function analysis. Considering that the oxidation state of Ta atom is +4, there is one unpaired $5d$ electron left per Ta that plays the most important role around the Fermi level. For a SD consisting of 13 Ta atoms, we need seven Wannier functions (without the spin degree of freedom) to fully accommodate these 13 unpaired $5d$ electrons. Accordingly, the Bloch states of the seven highest occupied energy bands are chosen to construct the Wannier functions. The spatial distributions of the resulting maximally localized Wannier functions are plotted in Fig. 2(b), which automatically separate into two groups. The one denoted by $|c\rangle$ concentrates at the central Ta atom with a typical d_{z^2} geometry. The remaining six Wannier functions distribute dominantly along the edge of the SD ($|s_{\alpha=1,\ldots,6}\rangle$), which can be viewed as the bonding orbitals of the surrounding Ta atoms. This Wannier function analysis gives a natural explanation for the two types of orbital textures observed by STM. In particular, it clarifies that the honeycomblike structure arises from a set of linear-shaped molecular orbitals.

These two different types of orbital textures were also observed in Ref. [24] and used as an indicator of the CDW gap. We note that previous STM mapping indicated an additional center-surrounding variation of the orbital texture for the deeper occupied states [24]. This feature presents in our experiment and calculation as well. These deep occupied states are associated with a different set of Wannier functions orthogonal to $|c\rangle$ and $|s_{\alpha=1,\ldots,6}\rangle$, which can be clarified using the same technique. However, those Wannier functions are irrelevant to the low-energy physics. By mapping out the low-energy orbitals, we also note that the previously employed one-band Hubbard model is implicitly based on the $|c\rangle$ orbital alone. Since this orbital is largely localized, it is susceptible to a Mott transition, giving rise to the UHB and LHB. However, it is important to note that the validity of the one-band Hubbard model is guaranteed only by a large Δ_{CDW}. When Δ_{CDW} is reduced, a one-band-to-multiband transition has to be considered, which in turn plays an important role in the collapse of the Mott phase.

IV. MOTTNESS COLLAPSE UPON Se SUBSTITUTION

To test the validity of the two-orbital-texture model, we further investigate the electronic structure of 1T-TaS_2 under external influence. A rather gentle perturbation to the 1T-TaS_2 structure is to modify the buckling of the S atoms around the central Ta, which is expected to affect the CCDW order. Experimentally this can be effectively realized through isovalent substitution of S by Se [6,7], which has a larger ionic size and is expected to increase the buckling of the surrounding S atoms. We have synthesized a series of Se-doped 1T-TaS_2 single crystals, and use these samples to map out the collapse of the Mott phase.

A. Phase transitions

Substituting S with Se is known to suppress the Mott-insulating phase in 1T-TaS_2 [6,7], which can be seen

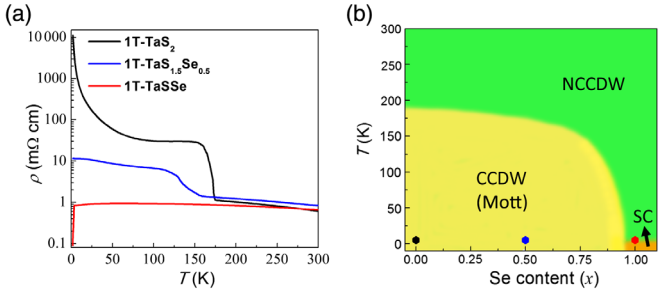

FIG. 3. (a) Temperature dependence of the in-plane resistivity of three typical 1T-$TaS_{2-x}Se_x$ samples. (b) Schematic electronic phase diagram of 1T-$TaS_{2-x}Se_x$ and the location of the three samples under STM measurements.

from the transport data. Figure 3(a) shows the in-plane resistance data of three 1T-$TaS_{2-x}Se_x$ samples that are used for discussion in this work. For the pristine 1T-TaS_2, there is a well-defined CCDW ordering around 180 K. Below this transition temperature, the resistance exhibits a typical insulating behavior. Clearly, Se substitution strongly suppresses this phase transition. For the $x = 0.5$ sample, the resistance jump around the phase transition point is weakened. For the $x = 1$ sample, it completely vanishes, and a flat resistance curve stays unperturbed until about 3 K, at which a sudden drop occurs. This is known to be a superconducting (SC) transition. Figure 3(b) displays the schematic phase diagram [7] and the location of the three samples under discussion.

We note that for Se substitution, due to its chemical similarity to S, the disorder effect is expected to be weak. This can be observed from the transport data: above the CCDW transition temperature, the resistance curves of the three samples almost coincide; the difference becomes evident only after the CCDW order kicks in.

B. Topographic change

How does Se substitution modify the CCDW order? Figure 4(a) displays a large area STM image on the surface of the $x = 0.5$ sample. Unlike the pristine sample, the surface structure now splits into domains with varied domain size and sharp boundaries in between [Fig. 4(a)], which resembles the so-called "mosaic" phase in 1T-TaS_2 induced by a voltage pulse in STM experiments [26,27]. Increasing the Se concentration from $x = 0.5$ to $x = 1$ creates more domain walls and defects, but the general topographic properties remain the same. A closer examination around the domain walls reveals both 30° rotational and translational mismatch between different domains [Figs. 4(b)and 4(d)]. According to the transport data, this domained phase in the $x = 1$ sample should adiabatically extend to the high-T NCCDW regime, in which the domains might shrink in size and the sharp domain boundaries melt into finite-width interdomain channels free of CCDW order [16]. However, close to the superconducting transition temperature, our STM image shows that the CCDW domains fill the whole space. Within a single domain, the CCDW superlattice retains the SD patterns as that in the undoped TaS_2 sample.

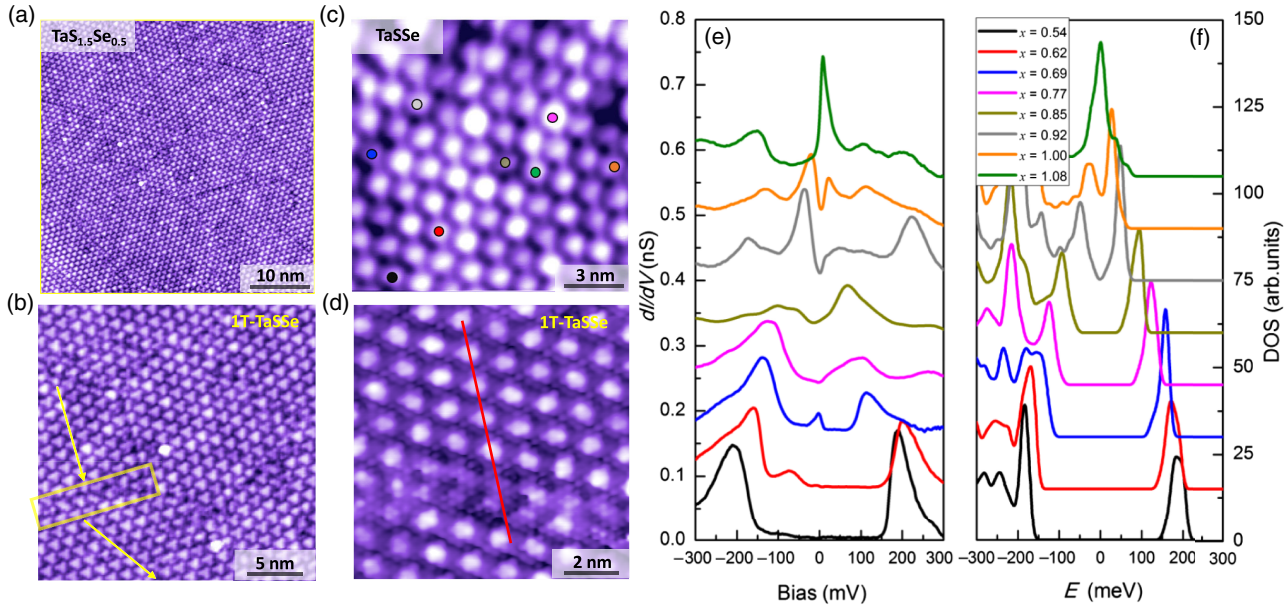

FIG. 4. Structural and electronic properties evolution of Se-substituted 1T-TaS_2. Topographic images acquired with $V_b = -500$ mV and $I_t = 20$ pA on the 1T-$TaS_{2-x}Se_x$ samples with the averaged Se concentration (a) $x = 0.5$ and (b)–(d) $x = 1$. (e) Local STM dI/dV spectroscopy measured at various locations on the surface as marked in (c). (f) DFT + U density of states of Se-substituted SDs in comparison with (e). In (b) and (d), the marks guide for eyes the rotational and translational mismatch in different domains.

C. Electronic inhomogeneity

STM dI/dV spectra are measured at various locations on the surface of the $x = 1$ sample [Fig. 4(c)], which are found to be surprisingly random. As we discuss in Sec. IV B, each bright spot in Fig. 4(c) corresponds to a single SD. The STM tip position is chosen to be close to the SD center, in order to prevent signals coming from multiple SDs. There is no visible domain wall within the range of Fig. 4(c) [cf. Fig. 4(d)], and we believe that all the measured positions belong to the same domain. By ordering them with respect to the gap size, we observe a complete evolution [Fig. 4(e)]. There are still areas (small in size) showing a spectrum similar to that in pristine 1T-TaS_2 with a nearly unperturbed Mott gap (black curve). Moving upwards, the Mottness gap shrinks continuously. With further shrinking of the Mott gap, a broad V-shaped gap forms near E_F, which looks reminiscent of the pseudogap in underdoped cuprates. The V-shaped gap also shrinks gradually, and a finite DOS appears at E_F, indicating the transition into a metallic state. Eventually the gap vanishes completely and a sharp peak emerges near E_F, which looks similar to the van Hove singularity (vHS) in overdoped cuprates.

A natural speculation on the origin of the inhomogeneous spectra is that the Se concentration in different SDs varies. We have calculated a series of SD structures by progressively replacing the S atoms with Se atoms. For a given Se concentration, the lowest-energy substitution configuration is determined, and the DFT structural relaxation confirms that the main effect of Se substitution is to increase the local buckling of the Ta-Se-Ta bonding geometry. We plot the DOS evolution as a function of Se concentration in Fig. 4(f), rendering a direct comparison with the STM dI/dV spectra. The overall evolution of the gap can be nicely reproduced in the theoretical simulation. Additionally, several distinct features, e.g., the U-shaped Mottness gap, the V-shaped pseudogap, and the sharp vHS-type peak, are also in good agreement.

Before explaining the underlying physics, it is worth addressing two possible concerns. Firstly, it is technically difficult to exclude the existence of other sources of inhomogeneity. However, given that our pristine sample is of very high quality, we believe that the predominant effect of Se substitution is to generate chemical inhomogeneity. The degree of inhomogeneity may rely on the sample preparation condition: a previous experiment has reported complete ordering of S/Se atoms in the TaSSe sample [8]. Secondly, our calculation considers only doping one single SD with a 2D periodic boundary condition. We assume that the local electronic properties are primarily governed by the intracluster coupling within the SD, and the chemical variation in the nearby SDs does not qualitatively change the local spectrum evolution. However, for the global or spatially averaged properties, such as transport behaviors and photoemission spectrum, the situation is beyond this local approximation, which could be an interesting question for further investigation.

D. Orbital shifts

Because of the spatial inhomogeneity, a 2D periodic pattern as shown in Fig. 2 no longer exists. To uncover the changes of the relevant orbitals, we perform a comparative analysis on the spectra linecut crossing multiple SDs before and after Se substitution.

In Fig. 5(a), we first present the linecut map of pristine 1T-TaS_2. The horizontal axis is the STM bias, ranging from -1000 to 1000 meV. The vertical axis is the position, measured along the line crossing five SDs. The LHB and UHB are evident at the bias of -200 and $+200$ meV. Along the position axis, they exhibit a periodic intensity variation, which peaks at the center of each SD (c) and weakens at the surrounding (s). The peak of the dI/dV shifts by half the period when moving the bias below (above) the LHB (UHB), indicating that the orbital component changes from $|c\rangle$ to $|s\rangle$.

For the doped sample [Fig. 5(b)], the orbital textures vary from one SD to another, and their spatial distributions become complicated. We first note that the deep CB or VB states, e.g., states around ± 1000 meV, remain largely periodic in space, exhibiting the similar textures as in the pristine sample, which again suggests that these states are not involved in the electronic phase transition. Around the Fermi level, the UHB can still be identified, which is bound by two clear gaps in most SDs. Despite a spatially varied magnitude, the UHB in general shifts to the lower energy, leaving a large gap between the CB, and almost touching the VB in some SDs. The strong narrow LHB peak now merges with the top of the VB. For some SDs, a narrow peak around the SD center appears as a remnant of the original LHB. Because of these orbital shifts, the Mott-insulator-to-metal transition occurs, and

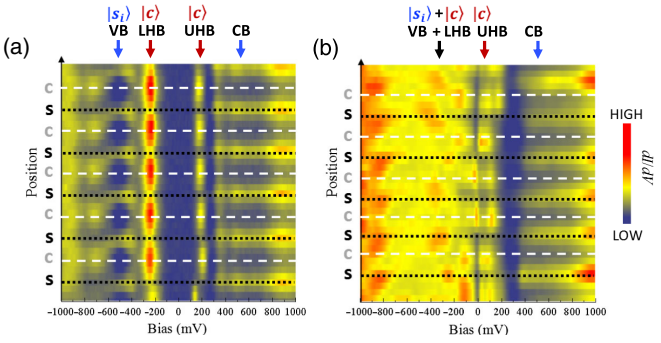

FIG. 5. STM line map. The dI/dV data for (a) $x = 0$ and (b) $x = 1$ in an extensive two-dimensional parameter space. The horizontal axis is the STM bias and the vertical axis is the position. The white dashed (black dot) lines mark the center (surrounding) of the SDs.

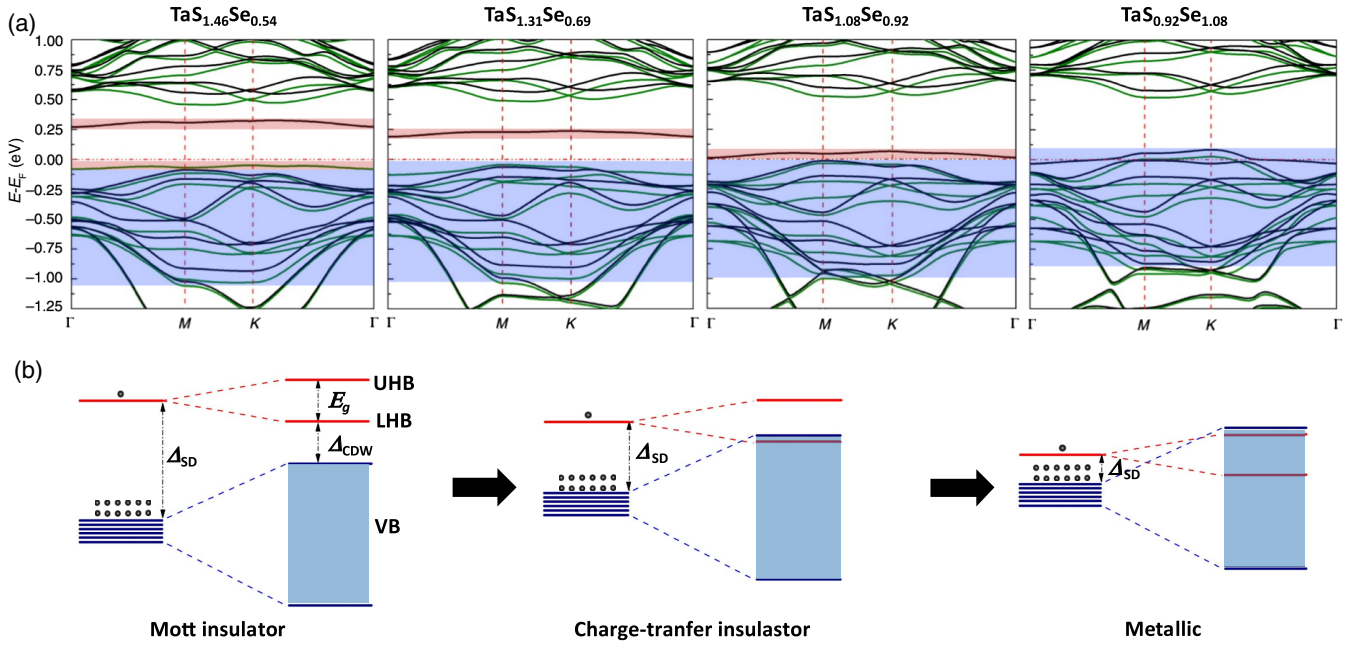

FIG. 6. (a) DFT + U band structures of Se substituted 1T-TaS_2. The meaning of the colors is the same as in Fig. 1(d). (b) Schematic energy level diagrams of the Mott insulating phase, the charge-transfer insulator phase and the metallic phase.

the surrounding orbitals play an equally important role in the low-energy physics.

These orbital shifts can be further compared with the DFT + U band structures. Figure 6(a) traces the band evolution as the Se concentration increases. The results indicate a progressive downward shift of UHB and LHB, in agreement with the STM line map. At low-doping concentration, despite a reduction of Δ_{CDW}, E_g stays unchanged as it is dictated by the effective Hubbard U of the $|c\rangle$ orbital alone. After the LHB touches the $|s_\alpha\rangle$-orbital bands, the Mott gap transforms into the charge-transfer-type gap because now the lowest-energy excitation is from the continuum band formed by the $|s_\alpha\rangle$ orbitals to the UHB formed by the $|c\rangle$ orbital. The gap size shrinks continuously upon further doping. According to the calculation, the critical point is reached at $x \approx 0.92$, where the charge-transfer gap becomes zero. Beyond this critical doping concentration, the UHB also sinks into the $|s_\alpha\rangle$-orbital bands, driving the system into the metallic regime. For the high-doping case, the $|c\rangle$ orbital and $|s_\alpha\rangle$ orbitals are strongly hybridized so that we can barely see the remnants of the narrow UHB around the Γ point at E_F. The excellent agreement between theory and experiment confirms the validity of the proposed transition mechanism, in which the orbital sequence determines the electronic property. We note that in the calculation no additional complexities, such as spin-orbit coupling, interlayer coupling, and disorder, are introduced. In addition, after Se substitution, Wannier function analysis shows that the geometry of the $|c\rangle$ and $|s_\alpha\rangle$ orbitals remains nearly unchanged. Therefore, we believe that the interplay between the $|c\rangle$ orbital and $|s_\alpha\rangle$ orbitals represents a universal origin of Mottness collapse in 1T-TaS_2.

V. THEORETICAL FORMALISM

To capture the essential physics, we propose a multi-orbital Hubbard model as formulated below:

$$H = \Delta_{\mathrm{SD}} \sum_I c_I^\dagger c_I + t_{cs} \sum_{I\alpha} (c_I^\dagger s_{I\alpha} + \mathrm{H.c.}) + \sum_{(I\alpha, J\beta)} t_{ss}^{I\alpha, J\beta} s_{I\alpha}^\dagger s_{J\beta} + U_c \sum_I c_{I\uparrow}^\dagger c_{I\downarrow}^\dagger c_{I\downarrow} c_{I\uparrow}, \quad (1)$$

where Δ_{SD} is the on-site energy difference between $|c\rangle$ and $|s_{\alpha=1,\ldots,6}\rangle$ generated by the formation of SD [Fig. 6(b)], and I, J indexes the SDs. The central orbital $|c\rangle$ experiences an effective on-site Coulomb repulsion U_c of the magnitude of LHB and UHB splitting ~0.25 eV, whereas the interaction terms for $|s_{\alpha=1,\ldots,6}\rangle$ are neglected considering they are less localized. Note that the Wannier function $|c\rangle$ is also a molecular orbital [Fig. 2(b)], and the associated Coulomb repulsion U_c is much smaller than its original 5d atomic-orbital counterpart as used in the DFT + U calculation. This difference was also addressed in Ref. [28]: a similar $U_c \sim 0.18$ eV was obtained by evaluating the projection of the Wannier function on the local d orbitals. The values of Δ_{SD} and the dominant hopping parameter (t) can be extracted by exploiting the same Fourier transformation as used in the Wannier function analysis (Table I).

TABLE I. Single-electron parameters from Wannier function analysis. The three columns correspond to the pristine 1T-TaS_2, 1T-$TaS_{2-x}Se_x$ ($x = 0.92$), and an artificially distorted 1T-TaS_2 that retains the same structure of 1T-$TaS_{2-x}Se_x$, respectively.

Unit (eV)	Pristine	Se doped	Distorted
Δ_{SD}	0.212	0.146	0.143
t_{sc}	0.162	0.099	0.105
t_{ss1}	0.150	0.175	0.171
t_{ss2}	0.091	0.089	0.087
t_{ss3}	0.072	0.021	0.013
t_{ss4}	0.050	0.047	0.043
t_{ss5}	0.042	0.043	0.036
t_{ss6}	0.042	0.032	0.030

For pristine 1T-TaS_2, the on-site energy of $|c\rangle$ is 0.21 eV higher than $|s_{\alpha=1,\ldots,6}\rangle$. The largest hopping amplitude is t_{sc} that is between $|c\rangle$ and $|s_{\alpha=1,\ldots,6}\rangle$, followed by several hopping processes among $|s_{\alpha=1,\ldots,6}\rangle$ (Fig. 7). Intercluster hopping is possible via t_{ss2}, t_{ss4} and t_{ss6}. The set of obtained parameters for pristine 1T-TaS_2 is susceptible to a Mott transition owing to a relatively large positive Δ_{SD}. For the Se-substituted sample, we present in Table I the parameters obtained from calculations on the ($x = 0.92$) supercell. Transition from the Mott phase to a metal is in principle described by Eq. (1) when the parameters vary, but solving Eq. (1) including the Hubbard term requires sophisticated many-body calculation that is beyond the scope of the current work. Nevertheless, a quick test can be made by keeping only the largest t_{ss} and t_{sc} terms and then diagonalizing the 7×7 Hamiltonian matrix. It shows that the highest eigenstate transforms from a dominant $|c\rangle$ character to a $|s_{\alpha=1,\ldots,6}\rangle$ character, which reflects the essence of the transition mechanism.

According to this effective model, we schematically summarize the overall electronic structure evolution in Se-doped 1T-TaS_2 [Fig. 6(b)]. The key ingredient is the organization of the two types of orbital textures $|c\rangle$ and $|s_{\alpha=1,\ldots,6}\rangle$ accompanied by the formation of the SD structures. The central orbital is isolated by the surrounding ones, making intercluster hopping of central-orbital electrons possible only via a high-order process. It is thus susceptible to a Mott transition when $|c\rangle$ is separated from $|s_\alpha\rangle$ in energy. On the other hand, the $|s_\alpha\rangle$ orbitals are extended with sizable hopping amplitude, naturally giving rise to a metallic phase when $|c\rangle$ and $|s_\alpha\rangle$ mix.

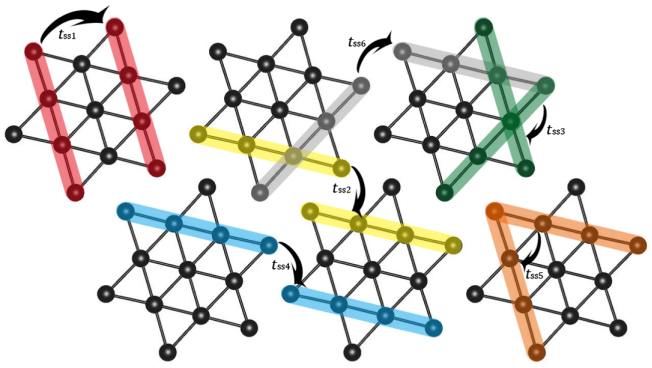

FIG. 7. Physical meaning of the hopping parameters between the surrounding orbitals listed in Table I.

We note that the in-plane hopping parameters summarized in Table I should not be confused with the out-of-plane hopping parameters discussed in Ref. [28], which were calculated by enforcing a periodic stacking structure. Although the in-plane hopping parameters appear comparable to the size of the out-of-plane hopping determined in Ref. [28] (ranging from 0.035 to 0.1 eV, depending on the stacking structure), their effects on the Mott transition are very different. The out-of-plane hopping leads to a significant increase of the $|c\rangle$-orbital bandwidth, which prevents a Mott-insulating ground state. Therefore, as argued in Ref. [28], in a real bulk 1T-TaS_2, such out-of-plane hopping processes must be quenched by stacking fault, which effectively localizes the electrons within the 2D plane, rationalizing from another perspective the 2D physics in 1T-TaS_2. In contrast, the in-plane hopping only slightly increases the $|c\rangle$-orbital bandwidth, because there is no direct hopping between two $|c\rangle$ orbitals, and they can be coupled only via high-order processes.

Previous dynamical mean-field theory calculations on the effective one-band Hubbard model [47–49] manually tuned the U value or, equivalently, the t/U ratio over a very wide range in order to trace the Mott-insulator-to-metal transition. As discussed above, the one-band Hubbard model is a down-folded version of our multiorbital model by integrating out the $|s_{\alpha=1,\ldots,6}\rangle$ orbitals. The down-folded U is affected not only by U_c associated with the $|c\rangle$ orbital, but also the energy separation between $|c\rangle$ and $|s_{\alpha=1,\ldots,6}\rangle$. In this sense, our work complements the previous speculation on a change of effective t/U ratio that induces the transition, and presents an explicit formalism to explain why the effective t/U ratio varies so greatly.

Finally, it is worth mentioning several points that bridge Se substitution with mechanical modulation. As we note in Sec. IV C, the main effect of Se substitution is to increase the local buckling of the Ta-Se-Ta bonding geometry. In calculation, we have also retained this buckled geometry, but change Se back to S. It is found that very similar band structure and single-electron parameters can be obtained (cf. the last two columns of Table I). In this sense, the possible structural modification as demonstrated by STM pulsing [26,27] may share the same physics as discussed above.

VI. CONCLUSION

Our experimental observations and first-principles calculations in 1T-TaS_2 reveal a new mechanism of Mottness collapse, which is fundamentally different from previously known examples such as charge-doping-induced collapse

in cuprates and pressure-induced collapse in weak Mott insulators. In the layered 1T-TaS_2, the isovalent substitution of S with Se does not induce additional charge carriers. Instead, it tunes the CDW order, and in turn drives the direct Mott gap into an effective "charge-transfer" gap. To the best of our knowledge, it is the first time that such a novel evolution between Mott gap and charge-transfer gap can be adiabatically accessed in the same material. Upon further substitution, after the charge gap fully collapses, the low-energy degrees of freedom include the Fermi-surface-forming itinerant carriers and fluctuating local magnetic moments, just like in heavy-fermion systems and iron pnictides or chalcogenides. It is thus interesting to ask whether this parent state for superconductivity is a heavy fermion liquid or a magnetic metal. An even more unique feature of 1T-TaS_2 is that the Mott physics is built upon a triangular lattice, in which spin frustrating is intrinsically coded. Therefore, the magnetic ground state of 1T-TaS_2 might be highly nontrivial [50]. We believe that the richness of the orbital-tunable electronic structure in Se-doped TaS_2 will shed important insights into several important topics of condensed-matter physics.

ACKNOWLEDGMENTS

This work is supported by NSFC under Grant No. 11534007 and MOST of China under Grant No. 2015CB921000. Q. S. and Z. L. are supported by Tsinghua University Initiative Scientific Research Program and NSFC under Grant No. 11774196. H. Y. is supported by NSFC under Grant No. 11474175. Z. L. and H. Y. also acknowledge support from the Thousand Talents Plan of China (for Young Professionals). N. W. and X. C. acknowledge the Strategic Priority Research Program (B) of the Chinese Academy of Sciences (Grant No. XDB04040100). This work is supported in part by the Beijing Advanced Innovation Center for Future Chip (ICFC).

S. Q. and X. L. contributed equally to this work.

[1] B. Sipos, A. F. Kusmartseva, A. Akrap, H. Berger, and L. Forró, and E. Tutiš, *From Mott State to Superconductivity in* 1T-TaS_2, Nat. Mater. **7**, 960 (2008).

[2] E. Morosan, H. W. Zandbergen, B. S. Dennis, J. W. G. Bos, Y. Onose, T. Klimczuk, A. P. Ramirez, N. P. Ong, and R. J. Cava, *Superconductivity in* Cu_xTiSe_2, Nat. Phys. **2**, 544 (2006).

[3] R. Ang, Y. Tanaka, E. Ieki, K. Nakayama, T. Sato, L. J. Li, W. J. Lu, Y. P. Sun, and T. Takahashi, *Real-Space Coexistence of the Melted Mott State and Superconductivity in Fe-Substituted* 1T-TaS_2, Phys. Rev. Lett. **109**, 176403 (2012).

[4] L. J. Li, W. J. Lu, X. D. Zhu, L. S. Ling, Z. Qu, and Y. P. Sun, *Fe-Doping-Induced Superconductivity in the Charge-Density-Wave System* 1T-TaS_2, Europhys. Lett. **97**, 67005 (2012).

[5] Y. Yu, F. Yang, X. F. Lu, Y. J. Yan, Y.-H. Cho, L. Ma, X. Niu, S. Kim, Y.-W. Son, D. Feng, S. Li, S.-W. Cheong, X. H. Chen, and Y. Zhang, *Gate-Tunable Phase Transitions in Thin Flakes of* 1T-TaS_2, Nat. Nanotechnol. **10**, 270 (2015).

[6] R. Ang, Y. Miyata, E. Ieki, K. Nakayama, T. Sato, Y. Liu, W. J. Lu, Y. P. Sun, and T. Takahashi, *Superconductivity and Bandwidth-Controlled Mott Metal-Insulator Transition in* 1T-$TaS_{2-x}Se_x$, Phys. Rev. B **88**, 115145 (2013).

[7] Y. Liu, R. Ang, W. J. Lu, W. H. Song, L. J. Li, and Y. P. Sun, *Superconductivity Induced by Se-Doping in Layered Charge-Density-Wave System* 1T-$TaS_{2-x}Se_x$, Appl. Phys. Lett. **102**, 192602 (2013).

[8] R. Ang, Z. C. Wang, C. L. Chen, J. Tang, N. Liu, Y. Liu, W. J. Lu, Y. P. Sun, T. Mori, and Y. Ikuhara, *Atomistic Origin of an Ordered Superstructure Induced Superconductivity in Layered Chalcogenides*, Nat. Commun. **6**, 6091 (2015).

[9] J. A. Wilson, F. J. DiSalvo, and S. Mahajan, *Charge-Density Waves and Superlattices in the Metallic Layered Transition Metal Dichalcogenides*, Adv. Phys. **24**, 117 (1975).

[10] C. B. Scruby, P. M. Williams, and G. S. Parry, *The Role of Charge Density Waves in Structural Transformations of* 1T-TaS_2, Philos. Mag. **31**, 255 (1975).

[11] P. Fazekas and E. Tosatti, *Electrical, Structural and Magnetic Properties of Pure and Doped* 1T-TaS_2, Philos. Mag. B **39**, 229 (1979).

[12] P. Fazekas and E. Tosatti, *Charge Carrier Localization in Pure and Doped* 1T-TaS_2, Physica B+C **99**, 183 (1980).

[13] B. Dardel, M. Grioni, D. Malterre, P. Weibel, Y. Baer, and F. Levy, *Temperature-Dependent Pseudogap and Electron Localization in* 1T-TaS_2, Phys. Rev. B **45**, 1462 (1992).

[14] B. Dardel, M. Grioni, D. Malterre, P. Weibel, Y. Baer, and F. Levy, *Spectroscopic Signatures of Phase Transitions in a Charge-Density-Wave System:* 1T-TaS_2, Phys. Rev. B **46**, 7407 (1992).

[15] J.-J. Kim, W. Yamaguchi, T. Hasegawa, and K. Kitazawa, *Observation of Mott Localization Gap Using Low Temperature Scanning Tunneling Spectroscopy in Commensurate* 1T-TaS_2, Phys. Rev. Lett. **73**, 2103 (1994).

[16] X. L. Wu and C. M. Lieber, *Hexagonal Domain-Like Charge Density Wave Phase of* TaS_2 *Determined by Scanning Tunneling Microscopy*, Science **243**, 1703 (1989).

[17] E. Lahoud, O. N. Meetei, K. B. Chaska, A. Kanigel, and N. Trivedi, *Emergence of a Novel Pseudogap Metallic State in a Disordered 2D Mott Insulator*, Phys. Rev. Lett. **112**, 206402 (2014).

[18] K. Aryanpour, W. E. Pickett, and R. T. Scalettar, *Dynamical Mean-Field Study of the Mott Transition in the Half-Filled Hubbard Model on a Triangular Lattice*, Phys. Rev. B **74**, 085117 (2006).

[19] L. Perfetti, P. A. Loukakos, M. Lisowski, U. Bovensiepen, H. Berger, S. Biermann, P. S. Cornaglia, A. Georges, and M. Wolf, *Time Evolution of the Electronic Structure of* 1T-TaS_2 *through the Insulator-Metal Transition*, Phys. Rev. Lett. **97**, 067402 (2006).

[20] H. Mutka, L. Zuppiroli, and P. Molinié, and J. C. Bourgoin, *Charge-Density Waves and Localization in Electron-Irradiated* 1T-TaS_2, Phys. Rev. B **23**, 5030 (1981).

[21] M. Bovet, S. van Smaalen, H. Berger, R. Gaal, L. Forr, L. Schlapbach, and P. Aebi, *Interplane Coupling in the*

Quasi-Two-Dimensional 1T-TaS_2, Phys. Rev. B **67**, 125105 (2003).

[22] K. Rossnagel and N. V. Smith, *Spin-Orbit Coupling in the Band Structure of Reconstructed* 1T-TaS_2, Phys. Rev. B **73**, 073106 (2006).

[23] P. Xu, J. O. Piatek, P.-H. Lin, B. Sipos, H. Berger, L. Forró, H. M. Rønnow, and M. Grioni, *Superconducting Phase in the Layered Dichalcogenide* 1T-TaS_2 *upon Inhibition of the Metal-Insulator Transition*, Phys. Rev. B **81**, 172503 (2010).

[24] D. Cho, Y.-H. Cho, S.-W. Cheong, K.-S. Kim, and H. W. Yeom, *Interplay of Electron-Electron and Electron-Phonon Interactions in the Low-Temperature Phase of* 1T-TaS_2, Phys. Rev. B **92**, 085132 (2015).

[25] T. Ritschel, J. Trinckauf, K. Koepernik, and B. Büchner, M. v. Zimmermann, H. Berger, Y. I. Joe, P. Abbamonte, and J. Geck, *Orbital Textures and Charge Density Waves in Transition Metal Dichalcogenides*, Nat. Phys. **11**, 328 (2015).

[26] L. Ma, C. Ye, Y. Yu, X. F. Lu, X. Niu, S. Kim, D. Feng, and D. Tománek, Y.-W. Son, X. H. Chen, and Y. Zhang, *A Metallic Mosaic Phase and the Origin of Mott-Insulating State in* 1T-TaS_2, Nat. Commun. **7**, 10956 (2016).

[27] D. Cho, S. Cheon, K.-S. Kim, S.-H. Lee, Y.-H. Cho, S.-W. Cheong, and H. W. Yeom, *Nanoscale Manipulation of the Mott Insulating State Coupled to Charge Order in* 1T-TaS_2, Nat. Commun. **7**, 10453 (2016).

[28] P. Darancet, A. J. Millis, and C. A. Marianetti, *Three-Dimensional Metallic and Two-Dimensional Insulating Behavior in Octahedral Tantalum Dichalcogenides*, Phys. Rev. B **90**, 045134 (2014).

[29] C. Ye, P. Cai, R. Yu, X. Zhou, W. Ruan, Q. Liu, C. Jin, and Y. Wang, *Visualizing the Atomic-Scale Electronic Structure of the* $Ca_2CuO_2Cl_2$ *Mott Insulator*, Nat. Commun. **4**, 1365 (2013).

[30] G. Kresse and J. Hafner, *Ab Initio Molecular Dynamics for Liquid Metals*, Phys. Rev. B **47**, 558 (1993).

[31] G. Kresse and J. Hafner, *Ab Initio Molecular-Dynamics Simulation of the Liquid-Metal-Amorphous-Semiconductor Transition in Germanium*, Phys. Rev. B **49**, 14251 (1994).

[32] G. Kresse and J. Furthmüller, *Efficiency of Ab Initio Total Energy Calculations for Metals and Semiconductors Using a Plane-Wave Basis Set*, Comput. Mater. Sci. **6**, 15 (1996).

[33] G. Kresse and J. Furthmüller, *Efficient Iterative Schemes for Ab Initio Total-Energy Calculations Using a Plane-Wave Basis Set*, Phys. Rev. B **54**, 11169 (1996).

[34] J. P. Perdew, K. Burke, and M. Ernzerhof, *Generalized Gradient Approximation Made Simple*, Phys. Rev. Lett. **77**, 3865 (1996).

[35] G. Kresse and D. Joubert, *From Ultrasoft Pseudopotentials to the Projector Augmented-Wave Method*, Phys. Rev. B **59**, 1758 (1999).

[36] N. Marzari and D. Vanderbilt, *Maximally Localized Generalized Wannier Functions for Composite Energy Bands*, Phys. Rev. B **56**, 12847 (1997).

[37] I. Souza, N. Marzari, and D. Vanderbilt, *Maximally Localized Wannier Functions for Entangled Energy Bands*, Phys. Rev. B **65**, 035109 (2001).

[38] A. A. Mostofi, J. R. Yates, Y.-S. Lee, I. Souza, D. Vanderbilt, and N. Marzari, *wannier90: A Tool for Obtaining Maximally-Localised Wannier Functions*, Comput. Phys. Commun. **178**, 685 (2008).

[39] A. I. Liechtenstein, V. I. Anisimov, and J. Zaanen, *Density-Functional Theory and Strong Interactions: Orbital Ordering in Mott-Hubbard Insulators*, Phys. Rev. B **52**, R5467 (1995).

[40] S. L. Dudarev, G. A. Botton, S. Y. Savrasov, C. J. Humphreys, and A. P. Sutton, *Electron-Energy-Loss Spectra and the Structural Stability of Nickel Oxide: An* LSDA + U *Study*, Phys. Rev. B **57**, 1505 (1998).

[41] F. Jellinek, F. Jellinek, and J. Less, *The System Tantalum-Sulfur*, J. Less-Common Met. **4**, 9 (1962).

[42] H. W. Myron and A. J. Freeman, *Electronic Structure and Fermi-Surface-Related Instabilities in* 1T-TaS_2 *and* 1T-$TaSe_2$, Phys. Rev. B **11**, 2735 (1975).

[43] A. M. Woolley and G. Wexler, *Band Structures and Fermi Surfaces for* 1T-TaS_2, 1T-$TaSe_2$, *and* 1T-VSe_2, J. Phys. C **10**, 2601 (1977).

[44] N. V. Smith, S. D. Kevan, and F. J. DiSalvo, *Band Structures of the Layer Compounds* 1T-TaS_2 *and* 2H-$TaSe_2$ *in the Presence of Commensurate Charge-Density Waves*, J. Phys. C **18**, 3175 (1985).

[45] F. Zwick, H. Berger, I. Vobornik, G. Margaritondo, L. Forró, C. Beeli, M. Onellion, G. Panaccione, A. Taleb-Ibrahimi, and M. Grioni, *Spectral Consequences of Broken Phase Coherence in* 1T-TaS_2, Phys. Rev. Lett. **81**, 1058 (1998).

[46] F. Clerc, C. Battaglia, M. Bovet, L. Despont, C. Monney, H. Cercellier, M. G. Garnier, P. Aebi, H. Berger, and L. Forró, *Lattice-Distortion-Enhanced Electron-Phonon Coupling and Fermi Surface Nesting in* 1T-TaS_2, Phys. Rev. B **74**, 155114 (2006).

[47] L. Perfetti, A. Georges, S. Florens, S. Biermann, S. Mitrovic, H. Berger, Y. Tomm, H. Höchst, and M. Grioni, *Spectroscopic Signatures of a Bandwidth-Controlled Mott Transition at the Surface of* 1T-$TaSe_2$, Phys. Rev. Lett. **90**, 166401 (2003).

[48] L. Perfetti, P. A. Loukakos, M. Lisowski, U. Bovensiepen, M. Wolf, H. Berger, S. Biermann, and A. Georges, *Femtosecond Dynamics of Electronic States in the Mott Insulator* 1T-TaS_2 *by Time Resolved Photoelectron Spectroscopy*, New J. Phys. **10**, 053019 (2008).

[49] J. K. Freericks, H. R. Krishnamurthy, Y. Ge, A. Y. Liu, and Th. Pruschke, *Theoretical Description of Time-Resolved Pump/Probe Photoemission in* TaS_2*: A Single-Band* DFT + DMFT(NRG) *Study within the Quasiequilibrium Approximation*, Phys. Status Solidi B **246**, 948 (2009).

[50] K. T. Law and P. A. Lee, *1T-TaS2 as a quantum spin liquid*, Proc. Natl. Acad. Sci. U.S.A. **114**, 6996 (2017).